simple three-state model. The HOMO of the complex is predominantly a bonding combination of the Au(6ŝ) state with the HOMO of pentacene, whereas the LUMO is an antibonding combination with the pentacene's LUMO. The remaining SOMO is a linear combination of the Au(6ŝ) state with both the HOMO (with antibonding character) and the LUMO (with bonding character). The apparent sideways bending of this state is purely an electronic effect. This bending and the nodal structure of the STM image are understood from the mixing of the HOMO and LUMO in the given phase relation, resulting in an enhanced amplitude on the side of the long axis of the pentacene molecule that is opposite from the Au atom. Furthermore, we find that the addition of the Au atom to the molecule is electrophilic, as there is a small net electron transfer to Au due to the larger electronegativity of the Au atom than of the pentacene molecule.

The calculations also show a stable adsorption configuration for the 5-gold-pentacene. The simulated STM image of this complex (Fig. 3B) is similar to the experimental image shown in Fig. 2J. The large difference in the apparent height between the ends of the complex is an electronic rather than a geometric effect, because the complex lies almost parallel to the surface.

Finally, DFT calculations on free gold-pentacene complexes without the NaCl/Cu(100) substrate reveal that these complexes are also stable and have similar geometric configuration and bond lengths, as well as orbitals and charge redistribution, to the adsorbed complexes. The main difference is an upward energy shift of the LUMO of the adsorbed complexes compared with a free complex because of their interaction with the occupied Cl^- 3p states.

Our DFT analysis confirms that the bond formation is an addition reaction of the gold atom to a pentacene's benzene ring, with a covalent character to create a radical complex. Aromatics usually prefer substitution over addition reactions that maintain their delocalized π-electronic system (*20*). However, in contrast to a reaction taking place in solution, the hydrogen atom in our case would have no alternate bonding partner.

Apart from the aspects of a contact formation, our findings also show new routes to selectively alter the electronic structure and chemical reactivity of large molecules with a delocalized electronic system. Control of the energetics of molecular resonances has been demonstrated before by the doping of a single molecule (*21*). The organometallic bond formation in our experiment even transforms a closed-shell molecule into a radical. This "engineering" of the orbital structure by creating different isomers controls both the nodal structure itself as well as the relative weight of the probability distribution in different parts of the molecule.

References and Notes

1. A. H. Flood, J. F. Stoddart, D. W. Steuerman, J. R. Heath, *Science* **306**, 2055 (2004).
2. B. C. Stipe *et al.*, *Phys. Rev. Lett.* **78**, 4410 (1997).
3. H. J. Lee, W. Ho, *Science* **286**, 1719 (1999).
4. S.-W. Hla, L. Bartels, G. Meyer, K.-H. Rieder, *Phys. Rev. Lett.* **85**, 2777 (2000).
5. J. R. Hahn, W. Ho, *Phys. Rev. Lett.* **87**, 166102 (2001).
6. J. Repp, G. Meyer, S. M. Stojković, A. Gourdon, C. Joachim, *Phys. Rev. Lett.* **94**, 026803 (2005).
7. J. Repp, G. Meyer, F. E. Olsson, M. Persson, *Science* **305**, 493 (2004).
8. D. M. Eigler, E. K. Schweizer, *Nature* **334**, 524 (1990).
9. J. Repp, G. Meyer, S. Paavilainen, F. E. Olsson, M. Persson, *Phys. Rev. Lett.* **95**, 225503 (2005).
10. X. H. Qiu, G. V. Nazin, W. Ho, *Phys. Rev. Lett.* **92**, 206102 (2004).
11. In the example shown, the bond was formed by running a tunneling current of $I = 2.5$ pA through the LUMO of the pentacene at a bias voltage of $V = +1.75$ V. The high bias voltage required for manipulation results from the electronic resonances of the adsorbate and is not a measure of the energy barrier of the process induced.
12. G. Pacchioni, L. Giordano, M. Baistrocchi, *Phys. Rev. Lett.* **94**, 226104 (2005).
13. In the present case, the two similar orbital images for both polarities of the bias voltage are not a result of the type of bipolar tunneling, as observed recently for a copper-phthalocyanine molecule on an alumina film (*14*). Also, tunneling at bias voltages of several volts results in IET-induced bond breaking even at an extremely low current of <1 pA. Thus, the HOMO and the LUMO of the complexes could not be measured experimentally.
14. S. W. Wu, G. V. Nazin, X. Chen, X. H. Qiu, W. Ho, *Phys. Rev. Lett.* **93**, 236802 (2004).
15. The Au-pentacene complex was adsorbed on a slab of four layers of Cu with 54 Cu atoms per layer and two layers of NaCl molecules in a super cell. All atoms except the two lowermost Cu layers were geometrically relaxed. The surface Brillouin zone was sampled using a 2×2 wave-vector mesh. The plane-wave basis set was truncated at a kinetic energy of 400 eV.
16. F. E. Olsson, M. Persson, *Surf. Sci.* **540**, 172 (2003).
17. G. Kresse, D. Joubert, *Phys. Rev. B* **59**, 1758 (1999).
18. G. Kresse, J. Furthmüller, *Phys. Rev. B* **54**, 11169 (1996).
19. J. Tersoff, D. R. Hamann, *Phys. Rev. Lett.* **50**, 1998 (1983).
20. K. P. C. Vollhardt, N. E. Schore, *Organic Chemistry* (W. H. Freeman & Co., New York, 2002).
21. R. Yamachika, M. Grobis, A. Wachowiak, M. F. Crommie, *Science* **304**, 281 (2004).

22. We thank R. Allenspach and S. Billeter for fruitful discussions. We acknowledge partial funding by the Academy of Finland; the Swedish Research Council (V.R.); the European Union projects CHIC, AMMIST, NANOSPECTRA, and NANOMAN; and allocation by computer resources by the Swedish National Allocations Committee.

10 February 2006; accepted 5 April 2006
10.1126/science.1126073

Carbon Nanotubes as High-Pressure Cylinders and Nanoextruders

L. Sun,[1] F. Banhart,[1]* A. V. Krasheninnikov,[2,3] J. A. Rodríguez-Manzo,[4] M. Terrones,[4] P. M. Ajayan[5]

Closed-shell carbon nanostructures, such as carbon onions, have been shown to act as self-contracting high-pressure cells under electron irradiation. We report that controlled irradiation of multiwalled carbon nanotubes can cause large pressure buildup within the nanotube cores that can plastically deform, extrude, and break solid materials that are encapsulated inside the core. We further showed by atomistic simulations that the internal pressure inside nanotubes can reach values higher than 40 gigapascals. Nanotubes can thus be used as robust nanoscale jigs for extruding and deforming hard nanomaterials and for modifying their properties, as well as templates for the study of individual nanometer-sized crystals under high pressure.

Because the covalent bond between two carbon atoms in graphite is one of the strongest known, a graphene plane consisting of a hexagonal arrangement of carbon atoms could be considered as a tearproof net at the nanoscale. Carbon nanotubes, which consist of cylindrically closed graphene sheets, therefore exhibit extreme mechanical properties that have been already demonstrated (*1–8*) and used in various applications (*9–11*). Although the rupture of nanotubes under axial tensile load has already been studied (*7*, *12*, *13*), their strength against internal pressure remains unexplored. Because nanotubes can be filled with various materials (*14–17*), the pressure-holding capacity of nanotubes may be tested by observing the behavior of encapsulated compressible materials upon tube contraction.

The contraction of nanotubes can be caused by knocking carbon atoms out from the tube lattice and allowing the atomic network to reconstruct. Such a contraction has been observed in spherical carbon onions under electron irradiation (*18*). Previous studies (*19–24*)

[1]Institut für Physikalische Chemie, Universität Mainz, 55099 Mainz, Germany. [2]Accelerator Laboratory, University of Helsinki, Post Office Box 43, FIN-00014, Finland. [3]Laboratory of Physics, Helsinki University of Technology, Post Office Box 1100, Helsinki 02015, Finland. [4]Advanced Materials Department, Instituto Potosino de Investigación Científica y Tecnológica, Camino a la Presa San José 2055, Col. Lomas 4a. sección, 78216 San Luis Potosí, México. [5]Department of Materials Science and Engineering, Rensselaer Polytechnic Institute, Troy, NY 12180–3590, USA.

*To whom correspondence should be addressed. E-mail: Banhart@uni-mainz.de

showed that nanotubes are self-healing structures under irradiation. Vacancies are mobile at sufficiently high temperature and coalesce to form divacancies, which ultimately mend by reconstruction of the lattice (*24*), reducing surface area and generating local tension in the graphene sheet. The collapse of hollow nanotubes under electron irradiation has been observed (*21*, *23*, *25*, *26*); however, the pressure effects experienced inside the cores during collapse have not been studied. In the present work, we observed the dynamics and compressibility of encapsulated nanowires inside collapsing nanotubes and demonstrated that even hard materials such as iron carbide or cobalt can be extruded under the pressures prevailing inside nanotubes.

Multiwalled carbon nanotubes (MWNTs) encapsulating Fe, Fe_3C, or Co nanowires were produced by means of a modified ethanol-metallocene–based chemical vapor deposition process. A solution was prepared by dissolving 3 weight percent of a metallocene (ferrocene or cobalt acetylacetonate) in ethanol (for Fe) or toluene (for Co); the solution was then sonicated and transferred to the reservoir of a sprayer (*27*–*29*). Subsequently, the metallocene solution was atomized and directed into a quartz tube in the presence of a high-purity Ar flow. The nanotubes grew inside the silica tube at 950°C for Fe and 850°C for Co. The filled nanotubes were dispersed ultrasonically in ethanol and placed onto grids for carrying out in situ electron microscopy experiments. Electron irradiation and imaging were done in a transmission electron microscope (TEM) (FEI Tecnai F-30) with a field emission gun and an acceleration voltage of 300 kV. A heating stage (Philips) was used to hold the specimens at a temperature of 600°C during the irradiation experiments and in situ imaging. At this temperature, defects in graphitic structures are mobile so as to prevent agglomeration that would lead to a rapid destruction of the nanotubes (*19*, *24*). Irradiation was carried out at beam current densities of 100 to 600 A/cm^2.

Figure 1 shows the evolution of a nanotube with nine shells containing a Fe_3C crystal under electron irradiation at 600°C. The initial configuration is shown in Fig. 1A. After 12 min of irradiation with an electron beam (approximately 80 nm in diameter and 200 A/cm^2 in intensity), the tube shrank and deformed the diameter of the Fe_3C crystal from 9 to 7 nm (Fig. 1B) and after another 9 min (Fig. 1C) to 6 nm. Because of the compressive deformation, the carbide wire increased in length. As the collapse of the tube started in the empty region, the wire slid through the hollow in the axial direction. The schematic in Fig. 1D shows the geometry. Some graphitic material aggregated inside the tube (Fig. 1, B and C), forming a new shell around the carbide crystal and some graphitic filaments in the collapsing hollow. The graphitic aggregates are due to the transfer of carbon interstitials into the tube (*21*). Initially, the end of the crystalline rod is often faceted (Fig. 1A), but aggregation of graphitic shells at the end of the crystal causes the appearance of a meniscus (Fig. 1, B and C). Therefore, the deformation and extrusion of the crystal are caused by the graphitic shells and not by a wetting effect. Heating alone does not result in the observed phenomenon. The collapse of the tubes and the extrusion of encapsulated material occur only under electron irradiation, not under heating. Additional heating of the specimen by the electron beam is negligible because the inelastic energy loss of the electrons is low and nanotubes are excellent heat conductors, so the transferred energy can dissipate into the environment.

The TEM image series (Fig. 2) shows the extent to which a Fe_3C crystal can be deformed inside the nanotube. Irradiation of the section at the end of the wire leads to a non-uniform collapse of the tube. The hollow noncollapsed part of the tube fills up with graphitic filaments (Fig. 2B). Carbon material migrates from the open side of the channel (top of each panel in Fig. 2) and aggregates to the end of the Fe_3C wire by closing the inner hollow with graphene sheets. Therefore, the number of shells increases locally. The tube now collapses in the region of the carbide crystal by deforming the crystal considerably (Fig. 2, D and E). The diameter of the Fe_3C wire decreases from 9 to 2 nm while the solid carbide is squeezed through the hollow core downward along the tube axis, as in an extrusion process. The final collapse of the tube pinches and cuts off the thinned wire (Fig. 2F) while the rest of the wire continues moving downward (the imaged section of the tube was slightly shifted during imaging). The deformation rate of the Fe_3C crystal is approximately 4 nm/min in the direction of the tube axis and 1 nm/min perpendicular to the axis. Qualitatively, the extrusion process (Figs. 1 and 2 for Fe_3C) is the same as when β-Co crystals (face-centered cubic) are encapsulated in nanotubes (fig. S1)

The compressive effect is also seen in the lattice spacings of the graphitic shells and the encapsulated crystals. In the nanotubes, a reduced spacing between the shells is seen close to the solid core. The spacing between the two innermost layers (next to the core) is 10 to 13% less than the spacing between the outer layers. Between the second and third shell, the reduction is typically less than 5%, whereas for all other shells no significant deviation from the value of graphite can be measured. The local pressure cannot be calculated in a straightforward way from the inter-shell spacing of the tube, because each shell resists outer pressure and the diameter of the shells is determined by the defect configuration. However, a change in lattice spacing in the encapsulated crystals can be used to estimate the local pressure, although the lattice resolution of the TEM is not sensitive enough to detect minute changes in spacings in this instance. In the Fe_3C nanocrystals, up to 6% compression in the radial direction was observed. For Co crystals in collapsing nanotubes, a compression of up to 3.5% was measured. Lattice distortions by shear forces were also detectable (fig. S2).

No visible crystallographic defects such as stable dislocations or twins were observed during the deformation of the crystals within the temporal resolution of this experiment (Fig. 1 and figs. S1 and S2). This is important because it shows that nanoscale crystals do not

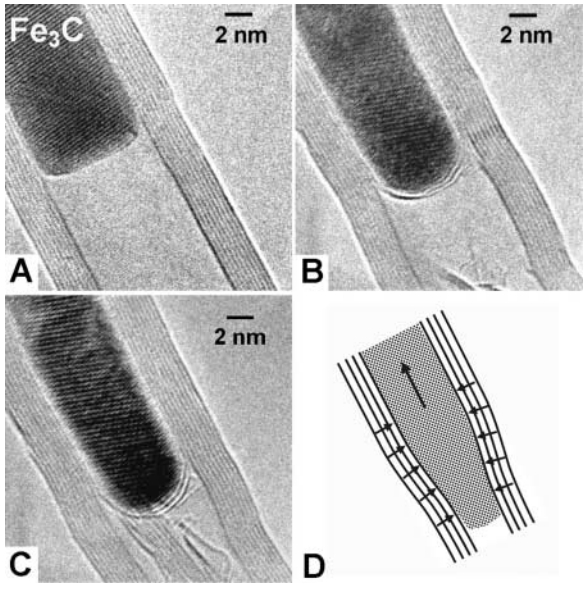

Fig. 1. MWNT with a Fe_3C crystal (dark region) in the inner core under electron irradiation at a specimen temperature of 600°C. The shrinkage of the tube leads to a deformation (thinning) of the Fe_3C crystal. Tubes before irradiation (**A**) and after 12 min (**B**) and 21 min (**C**) of irradiation are shown. The lattice fringes in (A) and in (B) and (C) originate from different sets of lattice planes because of a slight rotation of the tube under irradiation. (**D**) Simplified geometry of the system. Compressive forces (indicated by the small arrows) from the tube shells lead to a thinning of the crystal and its sliding along the tube axis (indicated by the large arrow).

deform in the same way as do macroscopic crystals, although the formation of defects has been observed in some metals encapsulated in carbon onions (*30*). Because the strain rate is low, we can consider that plastic deformation occurs above the theoretical shear stress rather than the yield stress as in bulk crystals. Such a behavior under plastic deformation is also a testimony to the large stresses that develop inside collapsing nanotubes. When the irradiation is interrupted, the compressive forces continue to have a slight effect for a short duration until the deformation stops. This technique allows for a direct observation of deformation dynamics in nanocrystals under large compression; however, the possible irradiation effects in the crystals also have to be taken into account.

In order to understand the mechanism of irradiation-mediated contraction of nanotube shells and to estimate the pressure inside the contracting tube, we used a continuum theory model in which the forces acting on the shells are functions of shell radii and inter-shell spacing (Fig. 3A). We used atomistic computer simulations to parameterize the model as described in the supporting online material. Knock-on displacements of carbon atoms in the energetic electron beam create vacancies and interstitials in the graphitic lattice of the nanotubes. In the metal and carbide cores, however, no considerable radiation effects occur because the displacement threshold energy in metals and carbides is higher than that in graphite. At 600°C, interstitials between the shells of MWNTs can migrate away from the contracting region where the pressure is high, so one can assume that no interstitials are left in the irradiated area. Metastable interstitial-vacancy complexes are also not stable at 600°C and will annihilate. Single vacancies are mobile enough to form divacancies (*24*), which are energetically favorable over single vacancies and are practically immobile (because the migration energy is more than 5 eV). Thus we can further assume that only double vacancies are present. Although all contracting shells should give rise to a pressure buildup in the inner core, it is instructive to evaluate first the pressure exerted only by the inner shell.

We calculated the total energy and the equilibrium atomic structure of single-walled carbon nanotubes (SWNTs) with various concentrations n of divacancies. Figure 3B shows the atomic network of a (10, 10) SWNT with $n = 0.05$. We found that the average equilibrium diameter $R_0(n)$ of the empty tube decreased linearly with n after relaxation because of the atomic network reconstruction. Having relaxed the atomic network for a particular n, we calculated the pressure P inside the SWNT as a function of nanotube radius R for various n (Fig. 3C). In practice, as the filling of the tube should increase R with respect to $R_0(n)$, we evaluated P numerically as the derivative of the total energy with respect to R for $R > R_0(n)$. For all n, P first increased linearly with R, and then showed a nonlinear regime. Finally, P abruptly dropped when the bonds near vacancies started breaking at the critical radius $R_c(n)$. We found that, for any n, the nonlinear dependence of P on R for $R_0 < R < R_c$ can be almost perfectly fitted by a square polynomial function [as in (*31*)].

Knowing the pressure as a function of the tube radius, one can calculate the maximum pressure inside the tube for any concentration of defects. For an incompressible inner core, P as a function of defect concentration is defined by the intersection of the vertical line drawn at the radius of the intact tube with the load curves. The pressure inside a SWNT as a function of n is shown in Fig. 3D. If we assume that the tube is filled with an incompressible material, there exists an upper limit on pressure, because the tube breaks at a certain concentration of vacancies. For a (10, 10) SWNT, the highest possible, double-vacancy concentration is $n \approx 0.06$. In reality, the highest vacancy concentration should be smaller, beacuse high experimental temperatures favor transitions between metastable configurations with close energies, resulting in the collapse of the tube. As follows from our simulations, the pressure inside a single shell can be as high as 20 GPa, and we are still not in the instability region (gray area in Fig. 3D).

To account for pressure buildup due to other shells, we calculated the total pressure P_{tot} inside MWNTs composed of two or more shells with divacancies. We assumed that the relations among tube radius, pressure, and double-vacancy concentration as calculated for the (10, 10) SWNT are qualitatively correct for nanotubes with any chiralities and diameters. We further assumed that the concentration of irradiation-induced defects is the same in all shells. To describe the forces between the shells, we adopted an analytical approach with parameters derived from experiments and used previously in a model of contracting graphitic shells in carbon onions (*32*). The balance of vacancy-induced and inter-shell forces, and the counter force from the incompressible material in the core in the MWNT, makes it possible to derive a system of nonlinear equations for equilibrium radii of all shells, which can be solved numerically.

The pressure P_{tot} in the inner core of MWNTs filled with an incompressible material (where the radius of the inner tube is equal to that of a pristine tube) is presented in Fig. 3D for various numbers of shells. P_{tot} increases because of additional contributions from other shells, and its value can be 40 GPa or higher. This value is slightly below the highest external pressure (60 GPa) seen to collapse nanotubes under experimental conditions (*33*). The

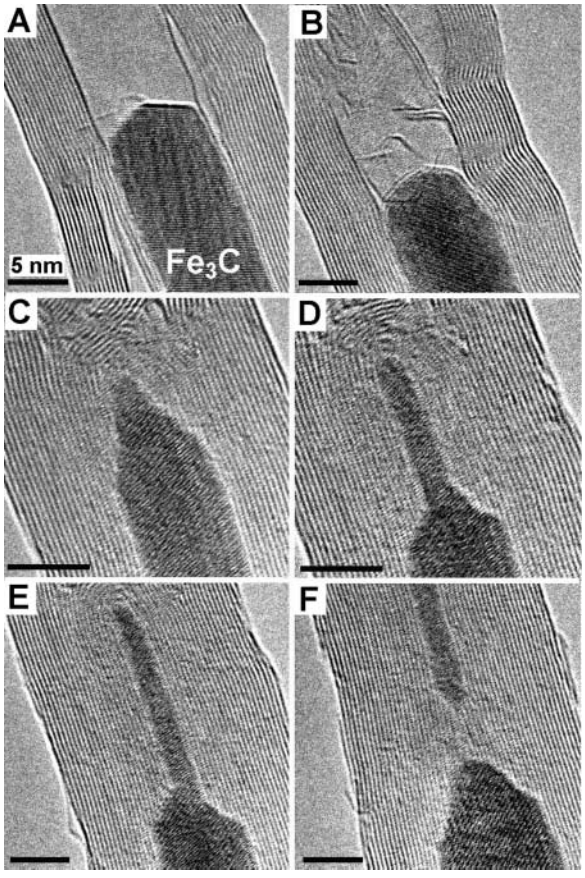

Fig. 2. Evolution of a MWNT partly filled with a Fe_3C nanowire under electron irradiation with an electron beam (about 60 nm in diameter and 200 to 400 A/cm² in intensity) during a total period of 50 min at a specimen temperature of 600°C. (**A**) Tube before irradiation. (**B** to **E**) Irradiation leads to a collapse of the tube and deformation of the Fe_3C crystal. (**F**) Tube collapse cuts off the thinned Fe_3C crystal. Different sets of lattice planes are seen in (A), (B), and (C) to (F). Scale bars, 5 nm.

pressure saturates quickly, and in practice does not change when the number of shells exceeds 6. This is because interstitials are absent in the high-pressure region because of the tubular geometry of the system, as a result of which the interstitials have a high probability to migrate away from the region with enhanced pressure. The open space and weak interaction between the shells allow for a decrease in shell radii and thus reduce P_{tot}. This also gives rise to a drop in inter-shell spacing, and the spacing is smaller the closer the shells are to the core. At a concentration of divacancies of 0.04, the inter-shell distance between the innermost and the next shell decreases by 15% relative to that of a pristine tube. Although a certain relaxation had already occurred when the experimental images were recorded, the measured inter-shell spacings of 10 to 13% match well with the theoretical value (unrelaxed situation). The effect of pressure on the lattice contraction of the encapsulated crystals can be estimated by using the compression modulus of bulk crystals. If we assume a pressure of 40 GPa and the measured compression modulus of bulk Fe_3C (the extrapolation according to the Birch-Murnaghan equation) (*34*), a reduction of lattice spacings of 5% can be expected. This value is close to the measured lattice compressions in Fe_3C (≤6%) and Co (≤3.5%).

Our results demonstrate the high strength of carbon nanotubes against internal pressure. The ultimate internal pressure (~40 GPa) that nanotubes can resist is only an order of magnitude below the pressure in the center of Earth (~360 GPa) or the highest pressure that has been achieved in diamond anvil cells (~400 GPa). The advantage of the present experiment is that individual nanometer-sized crystals can be studied in situ and deformed under high pressure, although irradiation effects in the crystals might occur and have to be considered. The behavior of the encapsulated crystals is monitored directly with high spatial and temporal resolution. Carbon nanotubes thus offer a template for use as compression/extrusion cells to study pressure-induced phase transformations and deformations of various solid nanomaterials.

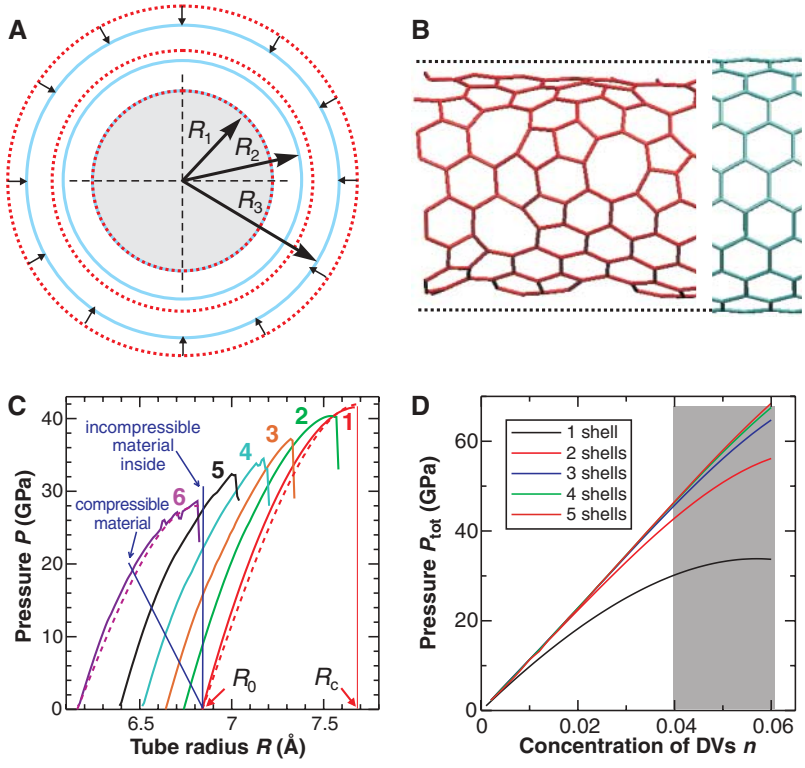

Fig. 3. (**A**) Schematic cross section of a MWNT contracting (indicated by the small arrows) because of the removal of atoms from the shells (solid blue circles) under the electron beam. The dashed red circles indicate the shells in the pristine tube. The inner core of the tube (gray circle) is filled with an incompressible material. Shell radii (R) are indicated by vectors. (**B**) Atomic networks of a pristine (10, 10) SWNT without (right) and with (left) double vacancies. There is a decrease in the average tube radius due to the reconstruction of the atomic network near vacancies. (**C**) Pressure versus tube radius (pressure-strain) curves corresponding to different divacancy concentrations n. Curve 1 corresponds to $n = 0$, 2 to $n = 0.007$, 3 to $n = 0.018$, 4 to $n = 0.028$, 5 to $n = 0.039$, and 6 to $n = 0.061$. Dashed lines are analytical fits to the simulation data. The straight blue lines illustrate the determination of pressure inside a SWNT filled with incompressible and compressible material; the intersections of the blue lines with pressure-strain curves give pressures for the corresponding divacancy concentrations. (**D**) Pressure inside a SWNT calculated as described above. The total pressure inside a MWNT with different numbers of shells is also shown as a function of n. DVs n, divacancy concentrations n.

References and Notes

1. M. M. J. Treacy, T. W. Ebbesen, J. M. Gibson, *Nature* **381**, 678 (1996).
2. E. W. Wong, P. E. Sheehan, C. M. Lieber, *Science* **277**, 1971 (1997).
3. J. P. Lu, *Phys. Rev. Lett.* **79**, 1297 (1997).
4. A. Krishnan, E. Dujardin, T. W. Ebbesen, P. N. Yianilos, M. M. J. Treacy, *Phys. Rev. B* **58**, 14013 (1998).
5. E. Hernández, C. Goze, P. Bernier, A. Rubio, *Phys. Rev. Lett.* **80**, 4502 (1998).
6. P. Poncharal, Z. L. Wang, D. Ugarte, W. A. de Heer, *Science* **283**, 1513 (1999).
7. M. Zhang *et al.*, *Science* **309**, 1215 (2005).
8. B. I. Yakobson, C. J. Brabec, J. Bernholc, *Phys. Rev. Lett.* **76**, 2511 (1996).
9. M. Cadek, J. N. Coleman, V. Barron, K. Hedicke, W. J. Blau, *Appl. Phys. Lett.* **81**, 5123 (2002).
10. A. B. Dalton *et al.*, *Nature* **703**, 423 (2003).
11. A. H. Barber, S. R. Cohen, H. D. Wagner, *Appl. Phys. Lett.* **82**, 4140 (2003).
12. M.-F. Yu *et al.*, *Science* **287**, 637 (2000).
13. M. Motta, Y. L. Li, I. Kinloch, A. Windle, *Nano Lett.* **5**, 1529 (2005).
14. P. M. Ajayan, S. Iijima, *Nature* **361**, 333 (1993).
15. S. C. Tsang, Y. K. Chen, P. J. F. Harris, M. L. H. Green, *Nature* **372**, 159 (1994).
16. Y. Maniwa *et al.*, *J. Phys. Soc. Jpn.* **71**, 2863 (2002).
17. Y. Gogotsi, N. Naguib, J. A. Libera, *Chem. Phys. Lett.* **365**, 354 (2002).
18. F. Banhart, P. M. Ajayan, *Nature* **382**, 433 (1996).
19. F. Banhart, *Rep. Prog. Phys.* **62**, 1181 (1999).
20. J. X. Li, F. Banhart, *Nano Lett.* **4**, 1143 (2004).
21. F. Banhart, J. X. Li, A. V. Krasheninnikov, *Phys. Rev. B* **71**, 241408 (2005).
22. F. Banhart, J. X. Li, M. Terrones, *Small* **1**, 953 (2005).
23. A. V. Krasheninnikov, F. Banhart, J. X. Li, A. S. Foster, R. M. Nieminen, *Phys. Rev. B* **72**, 125428 (2005).
24. A. V. Krasheninnikov, P. O. Lehtinen, A. S. Foster, R. M. Nieminen, *Chem. Phys. Lett.* **418**, 132 (2006).
25. P. M. Ajayan, V. Ravikumar, J.-C. Charlier, *Phys. Rev. Lett.* **81**, 1437 (1998).
26. N. G. Chopra, F. M. Ross, A. Zettl, *Chem. Phys. Lett.* **256**, 241 (1996).
27. F. Lupo *et al.*, *Chem. Phys. Lett.* **410**, 384 (2005).
28. R. Kamalakaran *et al.*, *Appl. Phys. Lett.* **77**, 3385 (1998).
29. M. Mayne *et al.*, *Chem. Phys. Lett.* **338**, 101 (2001).
30. J. Li, F. Banhart, *Adv. Mater.* **17**, 1539 (2005).
31. T. Xiao, K. Liao, *Phys. Rev. B* **66**, 153407 (2002).
32. M. Zaiser, *Mater. Res. Soc. Symp. Proc.* **540**, 243 (1999).
33. Z. Wang *et al.*, *Proc. Natl. Acad. Sci. U.S.A.* **101**, 13699 (2004).
34. J. Li *et al.*, *J. Phys. Chem. Minerals* **29**, 166 (2002).

35. Support from the Deutsche Forschungsgemeinschaft (grant BA 1884/4-1) is gratefully acknowledged. P.M.A. acknowledges support from NSF DMR grant on Inter-American Collaboration between the Rensselaer Polytechnic Institute and the Instituto Potosino de Investigación Científica y Tecnológica. We also thank the Consejo Nacional de Ciencia y Tecnología (CONACYT)–Mexico for scholarship (J.A.R.M.) and the following grants: 45772 (M.T.), 41464-Inter-American Collaboration (M.T., P.M.A.), 2004-01-013-SALUD-CONACYT (M.T.), and PUE-2004-CO2-9 Fondo Mixto de Puebla (M.T.). The authors thank the four reviewers of this paper for particularly useful comments.

Supporting Online Material

www.sciencemag.org/cgi/content/full/312/5777/1199/DC1
Materials and Methods
Figs. S1 and S2
References

4 January 2006; accepted 7 April 2006
10.1126/science.1124594